RSC Applied Polymers

ROYAL SOCIETY OF CHEMISTRY

PAPER

View Article Online
View Journal | View Issue

Cite this: *RSC Appl. Polym.*, 2025, **3**, 125

Synthesis and pH-responsive properties of bacteria mimicking hydrogel capsules

Veronika Kozlovskaya[a] and Eugenia Kharlampieva*[a,b]

The evolution of a non-spherical shape of microorganisms helped them survive by evading capture and digestion, which is crucial for their biological functioning. Synthetic imitation of the non-spherical shapes of various microorganisms and cells can enhance the ability of synthetic particulates to deliver therapeutics inside the body. Herein, we synthesized non-spherical polymer hydrogel microcapsules with bacteria-mimicking shapes, including prolate ellipsoid, peanut, and hourglass shapes similar to some pathogen microorganisms like *Staphylococcus aureus*, *Bacillus subtilis*, *Escherichia coli*, and *Corynebacterium diphtheriae*. The hydrogel shells were synthesized through a multilayer assembly of hydrogen-bonded poly(methacrylic acid) (PMAA) and non-ionic poly(*N*-vinylpyrrolidone) (PVPON) homopolymers on the surfaces of non-porous iron oxide microparticles of 2 μm in length. After covalent cross-linking of PMAA layers, followed by the release of PVPON at pH = 8 and the dissolution of the particle templates, curved rod-shaped (PMAA) multilayer hydrogel microcapsules with a pH-responsive shell were obtained. Attenuated total reflection-Fourier transform infrared spectroscopy (ATR-FTIR) analysis confirmed the covalent cross-linking of the shell and the release of PVPON from the capsule shell networks. The (PMAA) hydrogel capsules demonstrated excellent retention of their ellipsoid, peanut, and hourglass shapes after core dissolution in acidic solutions despite a nanothin (~40 nm) hydrogel membrane. Remarkably, all systems retained bacteria-like shapes in solutions at pH = 8, increasing in size by 20–30%, as confirmed by confocal fluorescence microscopy. All bacteria-like shaped microcapsules demonstrated homogeneous swelling in all directions regardless of the coating location at the initial particle perimeter, indicating similar cross-linking for all shapes and no effect of the iron oxide particle surfaces on the formation of the hydrogel shell. This work can help develop polymeric non-spherical particulates that are adaptable and on-demand for biomedical applications, including advanced targeting of pathological tissues and developing artificial cells with intelligent responses to environmental cues. Synthetic imitation of bacteria-like shapes and morphological flexibility demonstrated in this work using a multilayer assembly of polymer hydrogel capsules can bring new insights into the understanding and synthetic reproduction of properties essential for the synthetic particulates to evade the immune system and increase tissue targeting. These properties can be critical for developing unconventional particulates for controlled delivery and advanced imaging.

Received 21st April 2024,
Accepted 7th June 2024

DOI: 10.1039/d4lp00137k

rsc.li/rscapplpolym

Introduction

The evolution of a non-spherical shape of microorganisms helped them survive by evading capture and digestion, which is crucial for the biological functioning of cells, bacteria, and viruses.[1] For example, rod-shaped bacteria can stay in solution for longer under Brownian motion, unlike the spherical one, as an axial extension of a microorganism promotes more straightforward navigation through the liquid.[2] Hence, rod-shaped bacteria can move five-fold more efficiently than a spherical one of the same volume.[3] A non-spherical shape is also crucial for viral and bacterial infiltration of the body.[4–8] Furthermore, unlike a spherical one, the rod shape can promote stronger surface attachment under high shear stresses.[9] The rod-like shape was essential for many motile bacteria for optimal energy use, navigating Brownian forces and following chemical gradients.[10,11]

By imitating the non-spherical shapes of various microorganisms and cells, the ability of synthetic particulates to deliver therapeutics in the body can be enhanced by improving their vascular dynamics, circulation time, and tissue uptake.[12–17] Various non-spherical delivery particulates, including inorganic[18] and polymeric[19] particles, liposomes,[20]

[a]*Department of Chemistry, The University of Alabama at Birmingham, Birmingham, Alabama, 35294, USA. E-mail: ekharlam@uab.edu*
[b]*The Center for Nanoscale Materials and Biointegration, The University of Alabama at Birmingham, Birmingham, Alabama, 35294, USA*

polymer micelles,[21] and vesicles,[22] have been explored for their improved ability to deliver therapeutics to target body tissues.[12,23] For instance, rod-shaped polymeric particles were less phagocytosed by macrophages and dendritic cells than spherical ones.[24] The rod shape of particles could lead to reduced accumulation in the liver and spleen and facilitate particle passage to other organs in the body.[25,26] The prolate shape of synthetic ellipsoid polymer particles was shown to promote increased circulation in the bloodstream with enhanced tissue targeting.[27] Computational modeling of rod and hourglass (*i.e.*, curved rod) particle shapes also demonstrated the effect of these shapes on particle cell uptake.[28] These shapes are particularly attractive for a drug delivery vehicle as they mimic the shape of bacteria and budding yeast cells.

Besides the non-spherical geometry, morphological changes can be significant for biological function when rapid modifications in cell/microorganism morphology *via* altering their size and shape in response to environmental cues can better facilitate their survival.[4,29,30] Related to that, some bacteria can decrease or increase their size,[31] become longer or curved,[32] or change their diameter.[33] The red blood cells (RBCs) developed protective shape deformations from echinocyte to discocyte to stomatocyte to withstand destruction from viral and enzymatic attacks and osmotic changes.[34] Conversely, elongated carcinoma cells can become rounded to increase their motility and invasiveness.[35,36]

The low rigidity and flexibility of particulates were then shown to reduce the extent of phagocytosis and prolong circulation.[37,38] Using shape engineering technologies such as particle replication in non-wetting templates (PRINT),[39] stretching of films with embedded polystyrene spheres,[40] and template-induced printing,[41] highly cross-linked polymeric microparticles with well-defined geometries have been produced. The low rigidity of polymeric hydrogels was shown to control particle association with cancer cells and improve their accumulation at targeted sites.[37] For example, decreasing the elastic modulus of polyethylene glycol (PEG) gel nanoparticles to the kPa range increased their *in vivo* circulation.[37] Softer nanoliposomes were 2.6-fold more efficient at accumulating in 4T1 tumors than more rigid particles.[42]

Polymeric hollow particles (*i.e.*, capsules) made *via* layer-by-layer (LbL) sequential assembly of polymers on the surfaces of destructible microparticulate templates using electrostatic, hydrogen-bonding, and covalent interactions were demonstrated to be useful to replicate various shapes and sizes of the templates.[43–48] The low bending rigidity of thin polymer capsules is advantageous for mimicking non-spherical biological structures.[49] Thin polymeric shells can undergo dimensional changes easier than the particles of the same material with no cavity as the bending rigidity of a thin plate increases by three orders of magnitude with the thickness increase.[50,51] For example, hollow cubical 2 μm-sized multilayer capsules could squeeze through smaller 0.8 μm membrane pores.[52]

Single- or multi-polymer multilayer hydrogels are obtained by cross-linking LbL (*i.e.*, multilayer) shells.[53] When exposed to varied solution acidity, pH-sensitive hydrogel shells demonstrated the exceptional ability to drastically and reversibly change their properties *via* swelling or shrinking.[53,54] The covalent links stabilize the hydrogel capsule wall upon controlled core dissolution, while functional groups not involved in covalent bonding exhibit stimuli-responsive behavior.[54] Earlier, erythrocyte-like discoidal multilayer hydrogel capsules showed more efficient cell internalization than spherical capsules.[55] Discoidal capsules 7 μm in diameter made of poly(allylamine hydrochloride) (PAH) and cross-linked with glutaraldehyde[56] squeezed through a 5 μm glass capillary and recovered their original shape. Moreover, the elasticity of that discoidal capsule was much greater than the passage threshold for discoidal PRINT hydrogels, while the capsule interior resembled a cell with a flexible cell membrane. Hence, developing non-spherical polymeric hydrogel capsules using multilayer self-assembly[57] can facilitate new designs of 'intelligent' vehicles for nanomedicine and theranostics.[58,59] Simultaneously, synthetic imitation of the shape, morphological flexibility, and softness of bacteria can bring new insights into the understanding and synthetic reproduction of their properties, including immune system evasion and increased tissue targeting helpful for controlled delivery[60] and advanced imaging.[61]

Herein, we report on the synthesis of curved rod-shaped microcapsules with a hydrogel shell using a multilayer assembly of hydrogen-bonded poly(methacrylic acid) (PMAA) and poly(*N*-vinylpyrrolidone) (PVPON) on the surfaces of curved rod-shaped non-porous iron(III) oxide microparticles. The PMAA layers within the (PMAA/PVPON) multilayer coating templated on the iron oxide microparticles were cross-linked with ethylene diamine, and PVPON was released from the resultant (PMAA) multilayer hydrogel network at pH = 8. The thin (PMAA) multilayer hydrogel capsules were produced upon the dissolution of the iron oxide templates in hydrochloric acid solutions. The curved rod hydrogel microcapsule shapes investigated in the study included prolate ellipsoid, peanut, and hourglass (Fig. 1), which emulated the shape of bacteria (*e.g.*, diplococci and coccobacilli) and the shape of a budding yeast cell or growing bacterial cells[62] (*i.e.*, hourglass for *Staphylococcus aureus*, *Bacillus subtilis*, *Escherichia coli*, and *Corynebacterium diphtheriae*). We explored the retention of the initial shape after the template particle dissolution and the capsule shape and size changes in slightly acidic (pH = 5) and neutral (pH = 8) solutions due to the pH-sensitivity of the ultrathin $(PMAA)_n$ multilayer hydrogel shell of the capsules (the subscript n denotes the number of PMAA layers within the PMAA hydrogel shell). The results of this study can bring new insights into the development of biomaterials for future biomedical applications, including advanced targeting of cancers and the development of artificial cells that can adapt to environmental cues.

Experimental

Materials

Poly(methacrylic acid) (PMAA, average M_w 100 000 g mol^{-1}) was obtained from Polysciences Inc. Poly(ethyleneimine) (PEI,

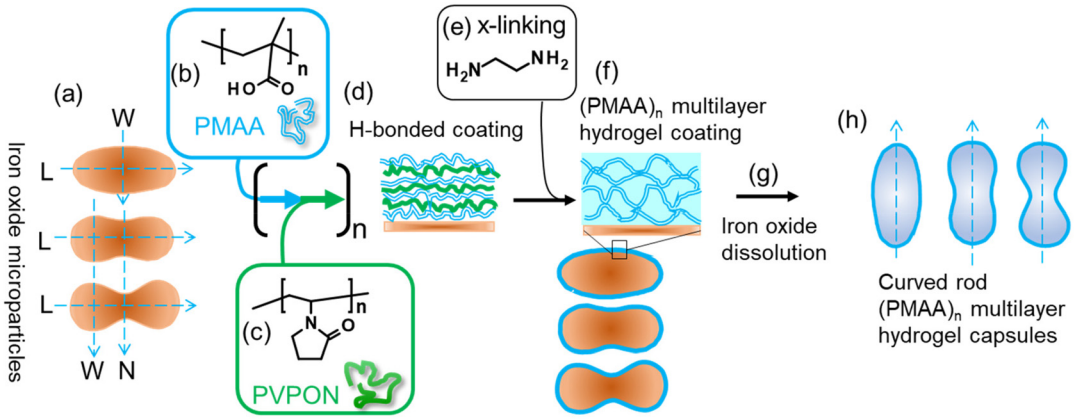

Fig. 1 Synthesis of curved rod $(PMAA)_n$ multilayer hydrogel capsules using layer-by-layer templating technique. (a) Iron oxide microparticles of curved rod shape were used as templating surfaces. Hydrogen-bonding polymers, (b) PMAA and (c) PVPON, were adsorbed on the particle surfaces *via* alternating polymer deposition until a desired number of (PMAA/PVPON) bilayers (n) was achieved. (d) The obtained $(PMAA/PVPON)_n$ hydrogen-bonded coating was cross-linked with (e) ethylene diamine, and PVPON layers were released from the coating at basic pH, leaving behind (f) the $(PMAA)_n$ multilayer hydrogel coating. (g) After the iron oxide templating particles were dissolved, the curved rod-shaped capsules with a $(PMAA)_n$ multilayer hydrogel shell (h) were obtained.

average M_w 25 000), poly(*N*-vinylpyrrolidone) (PVPON, M_w 58 000 g mol^{-1}), ethylenediamine (EDA), and iron(III) chloride hexahydrate ($FeCl_3$ $6H_2O$) were purchased from Sigma-Aldrich. 1-Ethyl-3-(3-(dimethylamino)propyl)-carbodiimide hydrochloride (EDC) was obtained from Chem-Impex International. Sodium hydroxide (NaOH), monobasic sodium phosphate (NaH_2PO_4), sodium sulfate (Na_2SO_4), and ethylene diamine tetraacetic acid sodium salt (EDTA) were purchased from Fisher Scientific. Ultrapure de-ionized water with a resistivity of 18 MΩ cm was used in all experiments. The Alexa Fluor 488 dihydrazide sodium salt (E_x/E_m = 488/510 nm) was purchased from Thermo Fisher. The Float-A-lyzer dialysis tubes (MWCO = 20 000 Da) were purchased from Repligen.

Synthesis of iron oxide (α-Fe_2O_3) microparticles of ellipsoid, peanut, and hourglass shapes

The iron oxide (α-Fe_2O_3) particles were synthesized by the sol–gel method developed by Sugimoto *et al.*[63,64] In a typical experiment, 9 mL of NaOH solution with 5.2 M was added to 10 mL of a well-stirred 2.0 M $FeCl_3$ solution in a 100 mL round-bottom flask within 3 minutes (200 rpm). Then, 1 mL of 0.06 M, 0.2 M, or 0.6 M Na_2SO_4 solution was added into the above solution of NaOH and $FeCl_3$ to achieve the ellipsoid, peanut, or hourglass-shaped microparticles, respectively. The resultant mixture was continuously agitated for 10 minutes until $Fe(OH)_3$ gel was formed. Afterward, the flasks were tightly capped with stoppers and aged in an oven at 100 °C for eight days. The obtained iron oxide microparticles were rinsed several times with DI water, air-dried, and collected.

Fluorescent labeling of PMAA

For fluorescent labeling, 132 mg EDC was added to 200 mg PMAA dissolved in 10 mL methanol and incubated for 30 min with occasional shaking. After that, 5 mg of Alexa Fluor 488 dihydrazide sodium salt was added, and the mixture was left for 24 hours under constant stirring in the dark. Then, the solution was dialyzed exhaustively against DI water using a Float-A-lyzer (MWCO 20 kDa). After no fluorescence traces could be detected in the dialysis water using fluorescence spectroscopy, the fluorescently tagged PMAA-Alexa488 solution was removed from the dialysis tube and freeze-dried (Labconco). To prepare fluorescently labeled PMAA capsules, 0.5 mg mL^{-1} PMAA solution was used for multilayer deposition within the last two bilayers.

Fabrication of PMAA multilayer hydrogel capsules of ellipsoid, peanut, and hourglass shapes

Hydrogen-bonded multilayers of $(PMAA/PVPON)_n$, where the subscript denotes the number of (PMAA/PVPON) polymer bilayers, were deposited on the PEI-coated iron oxide particles. For that, iron oxide particles were exposed to 1 mg mL^{-1} aqueous PEI solution at pH = 6 under mild shaking (100 rpm, Corning LSE Vortex Mixer) for 10 minutes. After that, the particles were separated from the polymer solution by centrifugation at 5000 rpm (1118 RCF) for 2 min using an Eppendorf MiniSpin microcentrifuge (a rotor radius of 4 cm) and rinsed two times with 0.01 M phosphate buffer at pH = 3 using centrifugation. After that, the PEI-coated cores were alternatively exposed to PMAA (0.5 mg mL^{-1}) and PVPON (0.5 mg mL^{-1}) polymer solutions at pH = 3 (0.01 M phosphate buffer) for 10 min each under mild shaking. Two buffer rinses were performed between each polymer layer. For the last two bilayers, fluorescently labeled PMAA-Alexa488 was used in place of PMAA to visualize the hydrogel capsules with confocal laser scanning microscopy (CLSM). After a desired number of PMAA/PVPON bilayers were deposited, the PMAA layers were covalently cross-linked. For that, the polymer-coated particles were first exposed to EDC solution (5 mg mL^{-1}, pH = 5, 0.01 M

phosphate buffer) for 40 min, followed by three rinses with 0.01 M phosphate buffer at pH = 5, and then to EDA solution (0.012 mL EDA mL^{-1} in 0.01 M phosphate buffer, pH = 5.8) for 6 hours under mild shaking. After that, the polymer-coated particles were rinsed three times with 0.01 M phosphate buffer at pH = 4.6 and exposed to pH = 8 (0.01 M phosphate buffer) for 12 hours under shaking to release PVPON from the PMAA multilayer network. Then, the iron oxide templates were dissolved by adding 8 M HCl solution to the polymer-coated particles. The yellow solution was then transferred to a Float-A-lyzer (MWCO 20 kDa) and dialyzed in DI water for two days. The 0.1 M EDTA (pH = 7.5) solution was added to the hydrogel capsules twice for 3 hours to completely chelate iron(III) ions, followed by dialysis in DI water for three days (MWCO 20 kDa). The capsule dispersions were stable and transparent for several hours. The capsules slowly settled to the Eppendorf tube bottom due to their micrometer size, with complete capsule sinking at the tube bottom after several (4–5) days, depending on the capsule thickness. However, using a vortex, the capsules could be easily redispersed in solution through periodic shaking.

Scanning electron microscopy (SEM)

SEM analysis was performed using a FEI Quanta™ FEG microscope at 10 kV. Samples were prepared by depositing a drop of a particle (or a capsule) suspension on a silicon chip and allowing it to dry at room temperature, covered with a Petri dish. Before imaging, dried specimens were sputter-coated with ~5 nm silver films using a Denton sputter-coater.

Attenuated total reflection-Fourier transform infrared spectroscopy (ATR-FTIR)

ATR-FTIR spectra of $(PVPON/PMAA)_{10}$ hydrogen-bonded and $(PMAA)_{10}$ hydrogel capsules of hourglass shape freeze-dried from aqueous solutions at pH = 3 and pH = 8, respectively, and of PVPON freeze-dried from pH = 3, were collected using a Bruker Alpha ATR-FTIR spectrometer.

ζ-Potential measurements

Surface ζ-potential measurements of inorganic templates of hourglass shape and $(PMAA)_{15}$ hydrogel capsules were performed using a Nano Zetasizer (Malvern). For pH-dependent ζ-potential measurements of the hydrogel capsules, their suspensions were settled, supernatants were removed, leaving hydrated capsules at the bottom, and 0.01 M phosphate buffer solutions at a desired pH were added, followed by alternating shaking and sonication for 1 min (Branson ultrasonic bath). A ζ-potential value was obtained by averaging three independent measurements (20 runs each).

Atomic force microscopy (AFM)

The capsule shell thickness was obtained from the topographic AFM images of capsules dried on Si wafer chips (0.5 cm × 0.5 cm) using an AFM Multimode 8 (Bruker). The height of the collapsed flat regions of capsules (a double wall of the capsule shell) was measured using capsule topography section profiles with NanoScope Analysis v150 software, and half of the height value was calculated as a single-wall capsule shell thickness.[65] The AFM silicon cantilevers with a tip radius of <10 nm and a resonance frequency of 300 kHz were used for imaging (NanoAndMore USA Corp.)

Confocal laser scanning microscopy (CLSM)

Confocal microscopy images of the PMAA multilayer hydrogel capsules were obtained with a Zeiss LSM 710 confocal microscope equipped with a 63× oil immersion objective. The excitation/emission wavelengths were E_x/E_m = 488/510 nm. For pH-dependent size change observations, a drop of a hollow capsule solution was added to a chamber in the Lab-Tek chambered coverglass (Electron Microscopy Sciences) and filled with 0.01 M phosphate buffer solutions at a desired pH value. Capsules were allowed to sediment for 3 hours before imaging. ImageJ (NIH) software was used to analyze the sizes of iron oxide microparticles from SEM images and the capsule dimensions in solutions with varied pH values.

Results and discussion

For mimicking bacterial shapes, iron oxide particles of a rod shape were selected (Fig. 1). The synthesis of the rod-shape iron oxide (α-Fe_2O_3) of a micrometer size was previously performed *via* the sol–gel process using the method developed by Sugimoto *et al.*[63,64] In this method monodisperse hematite particles are formed *via* two-step phase transformation of Fe$(OH)_3$ gel obtained by mixing iron(III) chloride and sodium hydroxide to β-FeOOH followed by aging of the latter to α-Fe_2O_3 at 100 °C for several days in the presence of sodium sulfate. This synthesis allowed for a controlled change of the particle from the rounded rod to the curved rod with a local curvature in the middle part of the particle by changing the concentration of sodium sulfate. In a typical experiment, a 5.2 M NaOH solution was added to a 2.0 M $FeCl_3$ solution and a 0.06 M Na_2SO_4 solution was added to the mixture to obtain particles with a rounded ellipsoid (rod) shape. Along with the prolate ellipsoid shape, we synthesized two additional shapes of iron oxide particles with a gradual increase in surface curvature near the locus of indentation: peanut- and hourglass-shaped particles (Fig. 1a). The indentation size at the center of the particle was finely tuned by increasing the Na_2SO_4 solution concentration from 0.06 M to 0.2 M for the peanut shape and 0.6 M for the hourglass shape.

The SEM analysis of the synthesized iron(III) oxide confirmed the rod-like shape and revealed non-porous smooth surfaces of the microparticles with a similar length (denoted as *L*) (Fig. 2). The analysis of particle dimensions shown in Table 1 demonstrates that the three types of particles had a similar average length of 2.5 μm with 2.1 ± 0.1 μm for the ellipsoid (Fig. 2a and b), 2.4 ± 0.2 μm for the peanut (Fig. 2c and d), and 2.5 ± 0.1 μm for the hourglass (Fig. 2e and f) shaped particles. The width of the particles denoted as *W* and measured at the maximum size of the middle part of the ellip-

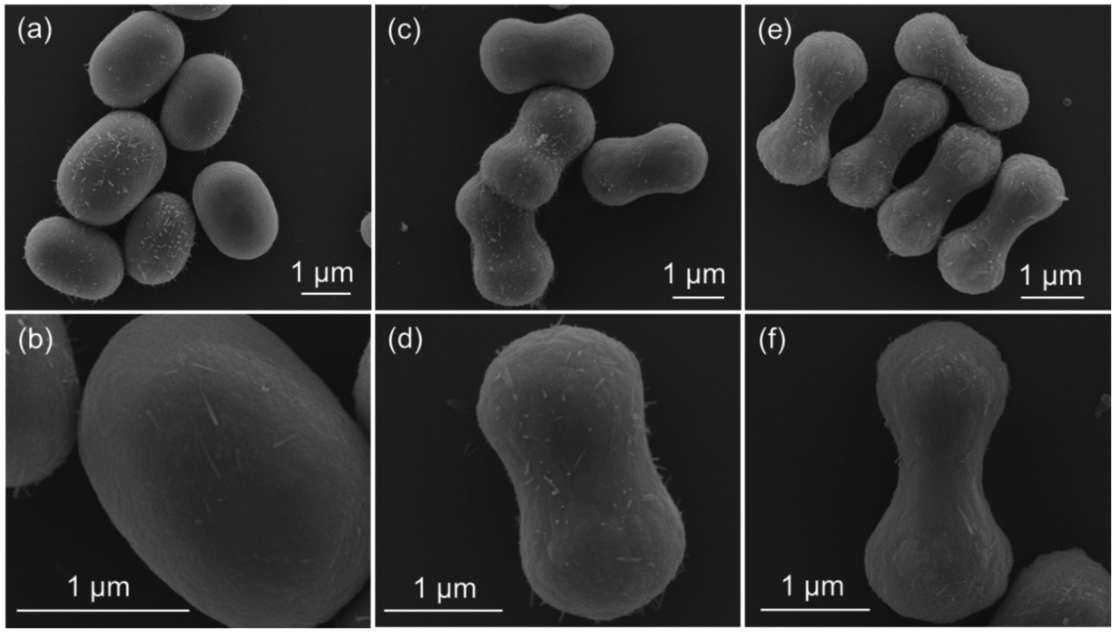

Fig. 2 SEM images of dry iron oxide template microparticles of (a and b) ellipsoid, (c and d) peanut, and (e and f) hourglass shapes.

soids and polar parts of the peanuts and hourglasses showed a gradual decrease to 86% for the peanut-shaped and 73% for the hourglass-shaped templates compared to the ellipsoid particles with the corresponding sizes of 1.5 ± 0.2 μm for the ellipsoid-, 1.3 ± 0.1 μm for the peanut-, and 1.1 ± 0.1 μm for the hourglass-shaped particles (Fig. 2b, d, f and Table 1). The analysis of the minimum width of the peanut and hourglass-shaped particles (denoted as *N*) revealed an increased curvature and an almost two-fold narrowing of the equatorial plane size for the hourglass-shaped iron oxide particles with the 'neck' diameter of 1.1 ± 0.1 μm and 0.7 ± 0.1 μm for the peanut (Fig. 2d) and hourglass (Fig. 2f) shapes, respectively (Table 1).

The assembly of the (PMAA/PVPON) multilayer on the surfaces of the particles (Fig. 1b–d) was carried out at pH = 3 to promote hydrogen bonds between the protonated carboxylic group (–COOH) of PMAA and the carbonyl group of the PVPON lactam ring (VPON).[45] The PMAA homopolymer could not be adsorbed onto the native surface of iron oxide particles. The ζ-potential measurements of the iron oxide surfaces revealed highly negative surface charge of the particles at basic (−59 ± 3 mV at pH = 8) and slightly acidic (−29 ± 2 mV at pH = 5) solution pH values and almost neutral (−4 ± 2 mV) at pH = 3 (Fig. 3a). The layer of PEI was adsorbed first on the iron oxide particle surfaces to reverse the particle surface charge to a positive value of 31 ± 3 mV at pH = 3 and promote the adsorption of the first PMAA layer (Fig. 3b). In previous reports, a similar PEI surface modification was shown to promote hydro-

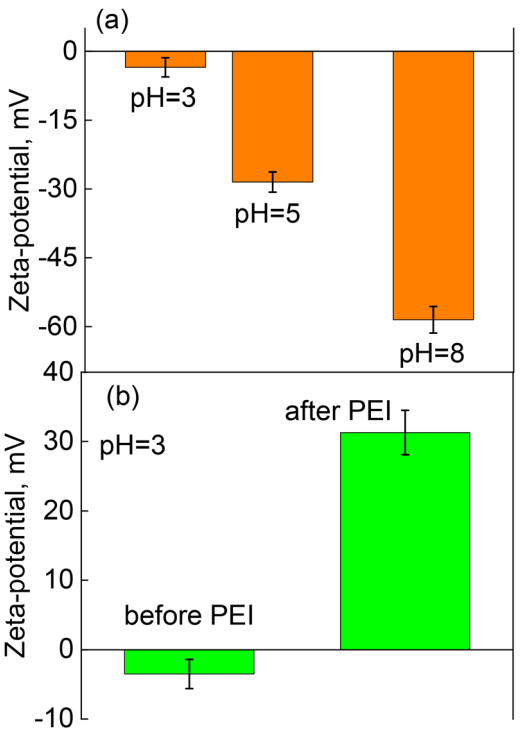

Fig. 3 Zeta-potential measurements of iron oxide inorganic particles in solution (a) before surface modification at pH = 3, pH = 5, and pH = 8, and (b) at pH = 3 before and after coating with PEI.

Table 1 Dimensions of iron(III) oxide template inorganic particles of curved rod shape including ellipsoid, peanut, and hourglass shapes

Dimensions	Ellipsoid	Peanut	Hourglass
Length, *L* (μm)	2.1 ± 0.1	2.4 ± 0.2	2.5 ± 0.1
Maximum width, *W* (μm)	1.5 ± 0.2	1.3 ± 0.1	1.1 ± 0.1
Minimum width, *N* (μm)	—	1.1 ± 0.1	0.7 ± 0.1

gen-bonded multilayer growth on the inorganic microparticles of cadmium or manganese carbonate.[66,67]

The hydrogen-bonded $(PMAA/PVPON)_n$ multilayer coating with a desired number of PMAA/PVPON bilayers (denoted as n) on the particles of three shapes was formed *via* the LbL assembly at pH = 3 (0.01 M phosphate buffer) using a centrifugation technique.[45] For fluorescent visualization, PMAA tagged with Alexa Fluor 488 was synthesized and deposited in the last two bilayers (see Experimental). The hydrogen-bonded (PMAA/PVPON) multilayer coating was converted into a (PMAA) multilayer hydrogel coating by cross-linking of PMAA layers with ethylenediamine at pH = 5 for 6 hours (Fig. 1e), followed by the release of PVPON layers from the network by the exposure of the core–shell particles to pH = 8 (Fig. 1f). After the dissolution of iron oxide inorganic templates in hydrochloric acid, the hollow $(PMAA)_n$ hydrogel capsules were obtained (Fig. 1g and h). Earlier, we had demonstrated that spherical, cubical, and discoidal $(PMAA)_n$ hydrogel capsules could be obtained by this method when initially templated on spherical silica, cubical manganese carbonate, and discoidal silicon inorganic templates, respectively.[46,67]

In general, increasing the number of layers in the multilayer capsule shell results in increased rigidity of the capsule wall. However, the hydrogel cross-link density for hydrogel capsules becomes equally important for maintaining the capsule shape after template removal. For example, thinner PMAA hydrogel cubical capsules exhibited face bulging after EDTA treatment at high pH.[67] Also, cubical (PMAA) multilayer hydrogel capsules with the same number of PMAA layers in the capsule shell but lower cross-link density (16 *versus* 41 MAA monomer units) lost their cubical shape upon the dissolution of the cubical inorganic template. At the same time, their more rigid 10-layer (PMAA) counterparts maintained the cubical shape after the core removal.[54]

The SEM image analysis of the hydrogen-bonded $(PMAA/PVPON)_{10}$ hollow capsules dried on silicon wafer surfaces confirmed a complete dissolution of the iron oxide particle cores in the HCl solution (Fig. 4a–c). Remarkably, the specific shapes of the particle templates can be seen even for the dried capsules, with most folds formed at the polar regions of the peanut (Fig. 4b) and hourglass (Fig. 4c) shaped capsules. Conversely, the hydrogel $(PMAA)_{10}$ capsules demonstrated very smooth morphology upon drying without any folds or creases due to the softness of the hydrogel network. Interestingly, the hourglass shape is clearly observed for the dried $(PMAA)_{10}$ hydrogel shells, unlike the ellipsoid and peanut shapes (Fig. 4d–f). The latter capsules are entirely spread over the silicon wafer surface, most probably due to capillary forces during drying, with their dry shapes becoming spherical and ellipsoid for the ellipsoid and peanut hydrogel capsules, respectively.

The polymer composition of the non-spherical multilayer capsules was analyzed with ATR-FTIR spectroscopy. Fig. 5 demonstrates the ATR-FTIR spectrum of freeze-dried 10-bilayer PMAA/PVPON hydrogen-bonded capsules obtained from the dissolution of the hourglass-shaped iron oxide microparticles. The two major peaks centered at 1700 cm^{-1} and 1640 cm^{-1} correspond to the carbonyl stretching vibrations of protonated carboxylic groups, –COOH, and carbonyl groups of the *N*-vinylpyrrolidone lactam ring, respectively (Fig. 5, spectrum 1).[68] The ATR-FTIR analysis also shows that the 1650 cm^{-1} band associated with the carbonyl groups in the pyrrolidone

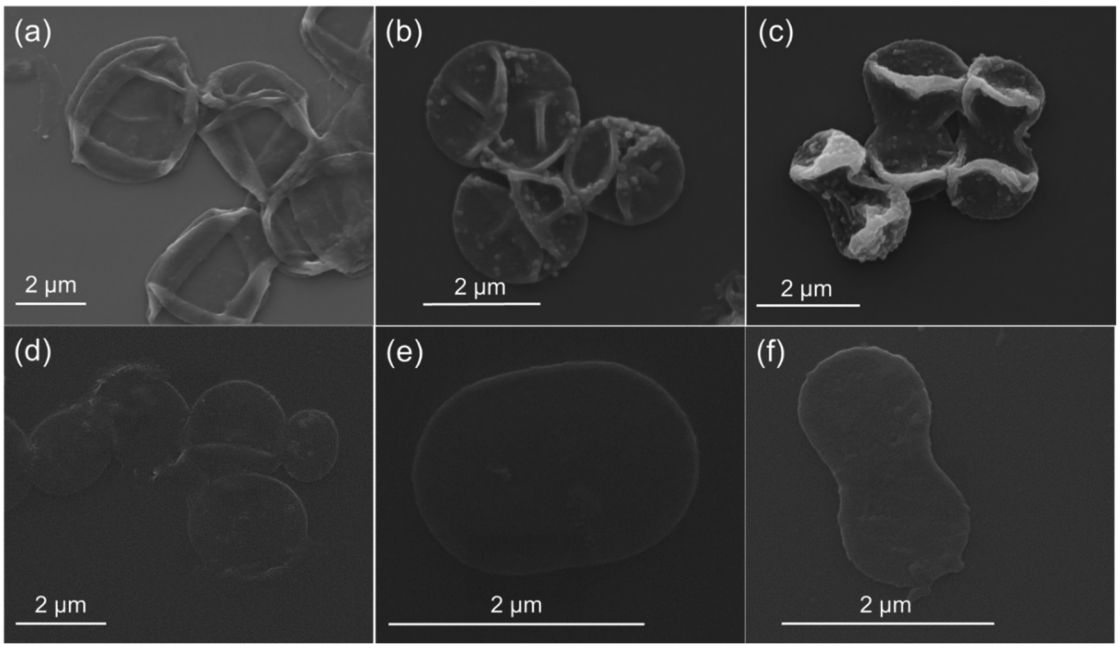

Fig. 4 SEM images of dry (a and b) hydrogen-bonded $(PMAA/PVPON)_{10}$ and (d–f) hydrogel $(PMAA)_{10}$ capsules of (a and d) ellipsoid, (b and e) peanut, and (c and f) hourglass shapes.

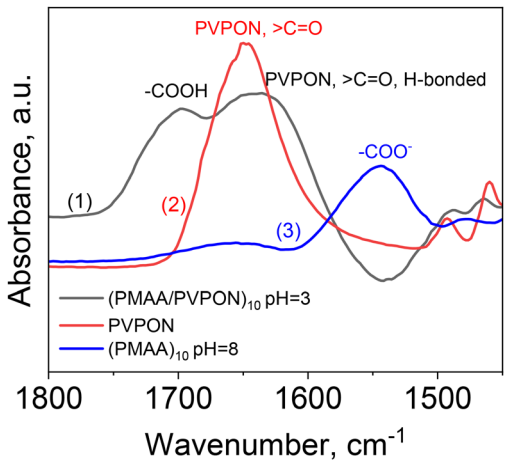

Fig. 5 ATR-FTIR spectra of freeze-dried hydrogen-bonded $(PMAA/PVPON)_{10}$ and hydrogel $(PMAA)_{10}$ hydrogel capsules (spectrum 1 and 3, respectively). The hydrogen-bonded capsules were freeze-dried from the capsule solution at pH = 3, while the hydrogel capsules from the capsule solution at pH = 8. PVPON homopolymer was freeze-dried from pH = 3 aqueous solution (spectrum 2).

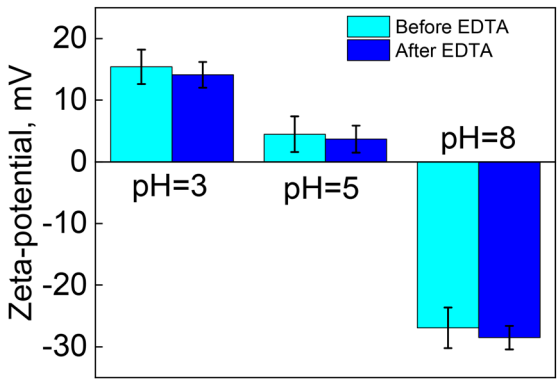

Fig. 6 ζ-potential measurements of $(PMAA)_{15}$ hydrogel capsules of hourglass shape at pH = 3, pH = 5, and pH = 8 in 0.01 M phosphate buffer before and after EDTA treatment.

rings in the free (non-hydrogen-bonded) PVPON homopolymer (Fig. 5, spectrum 2) is shifted to a lower frequency band of 1640 cm^{-1} when hydrogen-bonded with PMAA at pH = 3. The cross-linking of the hydrogen-bonded (PMAA/PVPON) coating with EDA resulted in amide bonds between the amine groups of EDA and the carboxylic groups of PMAA. The ATR-FTIR spectrum of the cross-linked $(PMAA)_{10}$ hydrogel capsules freeze-dried at pH = 8 demonstrates the band centered at 1660 cm^{-1} associated with amide I vibrations after cross-linking (Fig. 5, spectrum 3). The ionized PMAA carboxylic groups not involved in cross-linking can be seen in the hydrogel capsule spectrum at the band centered at 1545 cm^{-1} from the asymmetric stretching vibrations of the carboxylate groups (Fig. 5, spectrum 3).[69] The spectrum also shows the disappearance of the absorption band associated with PVPON (1640 cm^{-1}), confirming the formation of the PMAA multilayer hydrogel shell.[67]

As the non-spherical (PMAA) multilayer hydrogel capsules in this work were templated on iron oxide microparticles, the iron(III) ions produced upon the dissolution of the templates could affect the properties of the hydrogel shells, such as the pH-responsive surface charge and swelling of the capsules. Hence, all hydrogel capsule solutions were treated with EDTA solution (0.1 M, pH = 7.5) for three hours, followed by dialysis in DI water for three days to chelate the metal ions. The surface charge measurements of thick $(PMAA)_{15}$ hydrogel capsules before and after EDTA treatments showed a negligible effect from the possible iron(III) physical cross-linking of the PMAA network. Fig. 6 demonstrates ζ-potential measurements of the capsule suspensions in 0.01 M phosphate solutions at pH = 3, pH = 5, and pH = 8. The surface charge of $(PMAA)_{15}$ shells at pH = 3 was positive, with ζ-potential values of 15 ± 3 and 14 ± 2 mV for the capsules before and after the treatment, respectively. The hydrogel shell surface charge was close to neutral at pH = 5 for both EDTA-treated and non-treated hydrogel capsules, with the corresponding ζ-potential values of 5 ± 3 and 4 ± 2 mV (Fig. 6). The positive surface charge of the hydrogel particles at highly acidic pH is due to the protonated free amine groups in one-end attached crosslinker molecules, as reported earlier.[70] Likewise, the hydrogel capsules before and after the EDTA treatment showed negative ζ-potential at pH = 8 due to ionized PMAA carboxylates in the similar range of −27 ± 3 and −29 ± 2 mV, respectively (Fig. 6). The ζ-potential analysis of the capsule suggests that the inorganic core dissolution in hydrochloric acid followed by DI water dialysis results in almost a complete release of Fe^{3+} ions from the PMAA hydrogel, and the EDTA treatment may be necessary only if traces of the metal ions need to be removed. This observation was essential for favorably considering iron oxide non-spherical templates for hydrogel capsule synthesis instead of non-spherical calcium carbonates, with the latter having much higher binding energy with a carboxylic anion of ~249 kJ mol^{-1} compared to that of ~42 kJ mol^{-1} for Fe^{3+}.[71,72]

We investigated the pH-responsive behavior of the $(PMAA)_{15}$ hydrogel capsules with curved rod shapes using confocal microscopy. We found that all the capsule shapes maintained their non-spherical geometries after core dissolution and chelating the iron ions from the $(PMAA)_{15}$ network, showing three-dimensional (3D) hydrogel replicas of the non-spherical cores in solution at pH = 5 (Fig. 7a, c and e). This result demonstrates a favorable interplay between the hydrogel cross-link density and the hydrogel thickness, resulting in the capsule hydrogel wall being rigid enough to withstand the network volume transition due to the expansive entropy forces associated with polymer-solvent mixing and subsequent non-ionic swelling of the (PMAA) hydrogel at pH = 5. In our recent study, $(PMAA)_{10}$ cubical hydrogel capsules with a cross-link density of 41 monomer units between the cross-links lost their cube geometry, while the capsules having a cross-link density of 16 monomer units retained their cubical template shape during non-ionic swelling.[54]

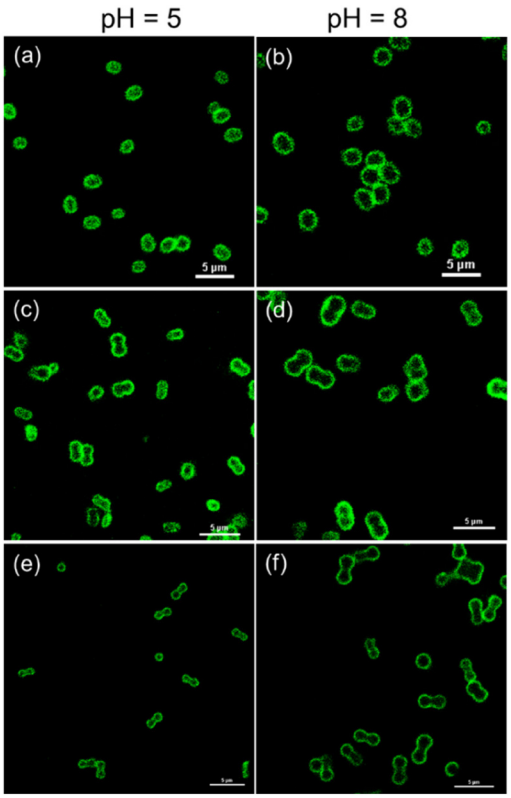

Fig. 7 CLSM images of $(PMAA)_{15}$ multilayer hydrogel capsules of (a and b) ellipsoid, (c and d) peanut, and (e and f) hourglass shape in solution at pH = 5 (left column) and pH = 8 (right column). The scale bar is 5 μm in all images.

Herein, the dry thickness of the $(PMAA)_{15}$ curved rod hydrogel shells was obtained from AFM images of dry capsules using the height analysis of the collapsed flat regions of a dry capsule[54] (Fig. 8). The shell thickness was similar for all three shapes and was 44 ± 1, 41 ± 1, and 41 ± 5 nm for ellipsoid-, peanut-, and hourglass-shaped capsules, respectively. The 3D rendering of the capsule surface morphology from 500 nm^2 areas of dry $(PMAA)_{15}$ hydrogel capsules shows overall smooth surfaces with nanosized domains from 5 nm (ellipsoid shape) up to 50 nm (peanut and hourglass shapes) that most probably replicate the surface morphology of the inorganic template surfaces (Fig. 2) and result from the hydrophobic coiling of PMAA at pH = 5 where the network surface charge is close to neutral (Fig. 6). Notably, the hydrogel capsule dimensions (Fig. 9) in solution at pH = 5 were similar to the sizes of the inorganic templates indicating a relatively rigid PMAA network under these conditions due to the presence of both covalent (two-end attached crosslinker molecules) and ionic cross-links (between negatively charged COO^- groups and positively charged protonated $-NH^{3+}$ groups from one-end attached crosslinker molecules)[53] (Tables 1 and 2).

Remarkably, all curved rod shapes of EDTA-treated $(PMAA)_{15}$ hydrogel capsules demonstrated distinct pH-induced swelling at pH = 8, as evidenced by the confocal fluorescence microscopy images of the capsules in solution (Fig. 7b, d and f). Higher magnification CLSM images of the peanut- and hourglass-shaped $(PMAA)_{15}$ capsules demonstrate that after being swollen, the hydrogel capsules maintain their initial shape upon a size increase (Fig. 10a and b). The fluorescence

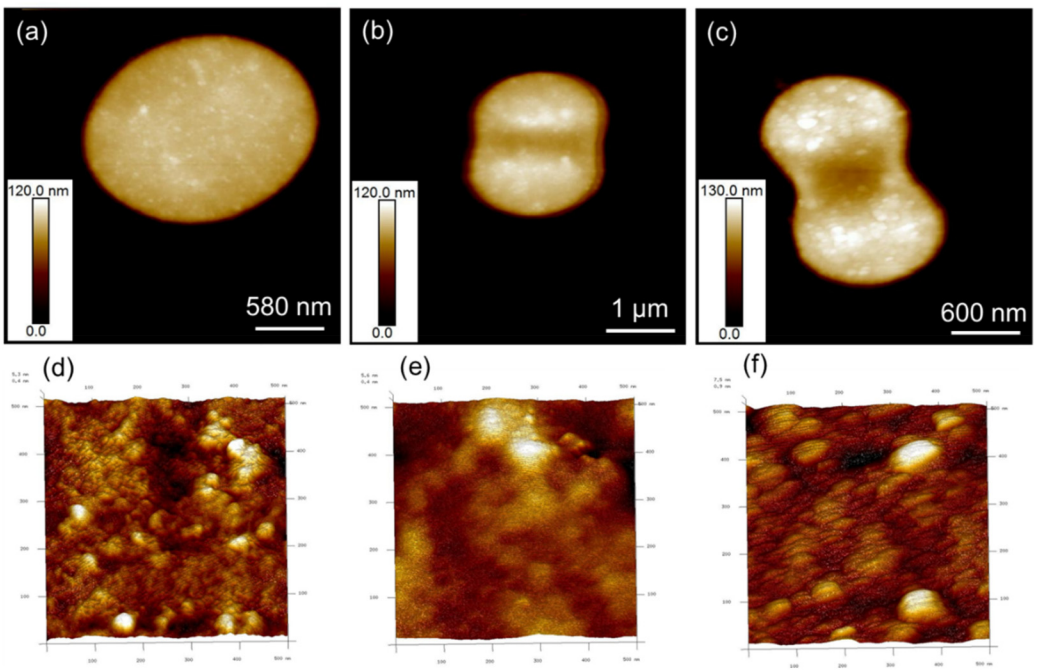

Fig. 8 AFM height images of dried $(PMAA)_{15}$ multilayer hydrogel capsules of (a) ellipsoid, (b) peanut, and (c) hourglass shape. Three-dimensional rendering of the capsule surface morphology from 500 nm^2 areas for (d) ellipsoid-, (e) peanut-, and (f) hourglass-shaped dry $(PMAA)_{15}$ hydrogel capsules.

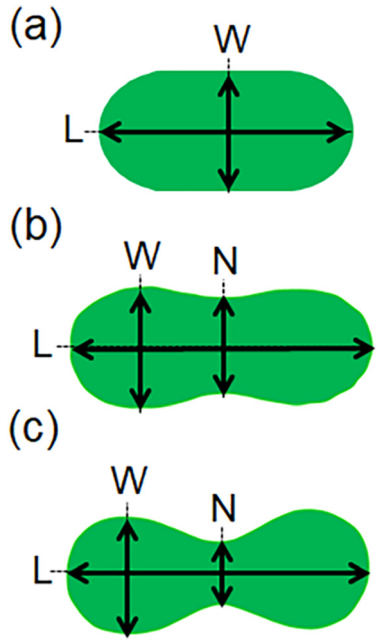

Fig. 9 The dimensional analysis of the curved rod $(PMAA)_{15}$ hydrogel capsules of (a) ellipsoid, (b) peanut, and (c) hourglass shape, including the capsule length, *L*, maximum cross-section width, *W*, and narrow cross-section width, *N*.

profile from a $(PMAA)_{15}$ hydrogel capsule in solution at pH = 8 shows a high fluorescence intensity from the capsule polymer shell, while almost no fluorescence signal can be observed from the capsule interior (Fig. 10c). These results indicate that the capsules are hollow with no polymer material in the capsule cavity, which agrees with the fact that the inorganic templates were not porous.

At basic pH, PMAA chains in this PMAA multilayer hydrogel are held together primarily by covalent linkages, while most ionic pairing is disrupted due to the gradual deprotonation of amine groups from one-end attached crosslinker molecules (pK_a of $-NH^{4+}$ is 9–10). For all shapes, the capsule dimensions obtained from CLSM image analysis increased by 20–30% (Table 2). For example, the swelling ratios of the ellipsoid hydrogel capsule length (S_L) and the maximum width (S_W) (Fig. 9), calculated as the ratio of the capsule size at pH = 8 to that at pH = 5, were $S_L = 1.28 \pm 0.03$ and $S_W = 1.20 \pm 0.01$, indicating the isotropic homogeneous swelling of the network in all directions (Table 2). In the case of the peanut-shaped capsules, the swelling ratios of the capsule length, maximum width, and minimum width (S_N) were $S_L = 1.24 \pm 0.02$, $S_W = 1.21 \pm 0.02$, and $S_N = 1.27 \pm 0.07$ with a negligible difference between them and in the same range as those found for the ellipsoid shaped hydrogel capsules (Table 2). The swelling ratios of the hourglass-shaped capsules were calculated to be $S_L = 1.29 \pm 0.02$, $S_W = 1.30 \pm 0.10$, and $S_N = 1.28 \pm 0.04$, which were also similar between themselves. This result also indicates homogeneous hydrogel swelling throughout the PMAA network regardless of the initial coating locus at the particle circumference. An insignificant increase in the swelling ratio values (up to 8%) for the hourglass-shaped hydrogel capsules compared to the swelling ratios of the ellipsoid and peanut shapes can be attributed to the slightly rougher surfaces of the hourglass hydrogel capsules as evidenced by AFM imaging (Fig. 8d–f). The similar swelling ratios across the three shapes of the $(PMAA)_{15}$ hydrogel capsules are also indicative of the similar cross-linking degree for all three shapes, implying that the chemistry of the iron oxide particle surfaces of the three shapes was the same and the particle shape did not affect the hydrogel formation. Earlier studies comparing hydrogen-bonded (tannic acid/polyvinylpyrrolidone) cubical and spherical capsules reported the cubical ones to be softer than their spherical counterparts when the capsule's small contact area deformations were probed.[73] In that case, the difference in capsule shell rigidity was attributed to unfavorable pore formation due to CO_2 release upon core dissolution.

Due to the isotropic hydrogel swelling, no capsule shape change was observed for any curved rod-shaped capsules studied here, but the capsule size changed (Fig. 7 and 10). All curved rod-shaped (PMAA) hydrogel capsules demonstrated a reversible dimension increase/decrease when the solution pH was alternated between pH = 8 and pH = 5 without changes in capsule shape. Previously, pH-induced swelling of the cubical $(PMAA)_{13}$ hydrogel capsule shell resulted only in partial shape reversibility.[68] Conversely, the pH-swelling-induced discoidal-to-ellipsoidal shape oscillations of $(PMAA)_{15}$ hydrogel capsules where only covalent cross-links were present in the network demonstrated complete shape recovery.[55] Importantly, hydrogel capsule shell stiffness was demonstrated to be crucial in the reversibility of capsule dimensional changes.[55] Thus, for example, dimensional changes of small-to-large cubical capsules of a more rigid $(PMAA\text{-}PVPON)_5$ hydrogel were utterly reversible, enduring the stresses due to hydrogel shell swelling. Conversely, thinner $(PMAA)_{20}$ cubical capsules bulged irreversibly at the cubical faces when swollen and shrunken back.[67,68]

Table 2 Capsule dimensions for $(PMAA)_{10}$ curved rod hydrogel capsules at pH = 5 and pH = 8, and the corresponding swelling ratios (*S*) expressed as the ratio of the capsule size at pH = 8 to that at pH = 5

	Ellipsoid		Peanut			Hourglass		
	L, μm	*W*, μm	*L*, μm	*W*, μm	*N*, μm	*L*, μm	*W*, μm	*N*, μm
pH = 5	2.12 ± 0.15	1.50 ± 0.11	2.47 ± 0.21	1.36 ± 0.11	1.05 ± 0.0.09	2.41 ± 0.18	1.05 ± 0.09	0.71 ± 0.08
pH = 8	2.68 ± 0.15	1.84 ± 0.14	3.14 ± 0.26	1.70 ± 0.11	1.41 ± 0.0.18	3.09 ± 0.29	1.52 ± 0.11	0.94 ± 0.08
S	1.28 ± 0.03	1.20 ± 0.01	1.24 ± 0.02	1.21 ± 0.02	1.27 ± 0.07	1.29 ± 0.02	1.30 ± 0.10	1.28 ± 0.04

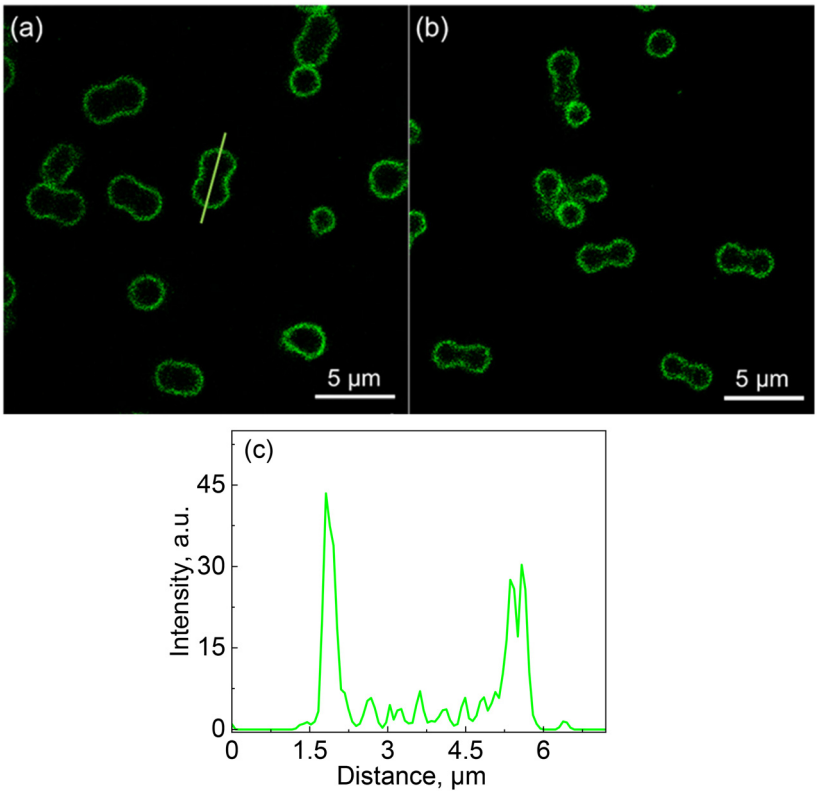

Fig. 10 High-magnification CLSM images of $(PMAA)_{15}$ multilayer hydrogel capsules of (a) peanut and (b) hourglass shapes in solution at pH = 8. (c) A fluorescence profile from the peanut shape capsule in solution at pH = 8 shown in (a).

Conclusions

Herein, we synthesized non-spherical polymer hydrogel microcapsules with bacteria-mimicking shapes, including prolate ellipsoid, peanut, and hourglass shapes similar to some pathogen microorganisms like *Staphylococcus aureus*, *Bacillus subtilis*, *Escherichia coli*, and *Corynebacterium diphtheriae.* The hydrogel shells of the capsules were realized through a multilayer assembly of the hydrogen-bonded weak anionic polyelectrolyte PMAA and the non-ionic polymer PVPON on the surfaces of non-porous Fe_2O_3 microparticles with a length of 2–2.5 μm. The covalent cross-linking of PMAA layers in the coating was followed by the release of PVPON at basic pH and the dissolution of the particle template in acidic solutions. This approach left behind curved rod hydrogel microcapsules with a pH-responsive capsule membrane. The low acidity (8 M HCl) used to dissolve the template microparticles did not affect the cross-linked PMAA multilayer hydrogel shell, which is stable under these conditions. However, in the case of using other polymer pairs and different cross-linking reagents for the preparation of the curved rod hydrogel capsules, the chemical stability of the polymers and crosslinkers, as well as interpolymer interactions under low acidity should be considered when using the reported approach. The $(PMAA)_{10}$ capsules demonstrated excellent retention of their ellipsoid, peanut, and hourglass shapes after core dissolution, as confirmed by SEM and CLSM analyses, despite a nanothin hydrogel membrane with a dry thickness of ~40 nm as measured using AFM imaging. ATR-FTIR analysis confirmed the covalent cross-linking of the shell and the release of PVPON from the capsule shell networks. The ζ-potential measurements of the capsules in solutions revealed pH-responsive properties of the capsule hydrogel shell where the positive and negative surface charges were reversibly switching between pH = 3 and pH = 8, respectively. At the same time, an almost neutral surface charge was attained at pH = 5 due to additional ionic pairing within the network under these conditions. Remarkably, all the shells retained bacteria-like shapes while exposed to solutions at pH = 8, as evidenced by confocal fluorescence microscopy. The non-spherical capsules increased in size by 20–30% in solutions at pH = 8. Homogeneous PMAA multilayer hydrogel swelling of all bacteria-like shaped microcapsules, regardless of the coating location at the particle perimeter, indicated similar cross-linking for all three shapes and no effect of the iron oxide particle surfaces of the three shapes on the hydrogel shell formation. This work can help develop polymeric non-spherical particulates that are adaptable and on-demand for biomedical applications, including advanced targeting of pathological tissues and developing artificial cells with intelligent responses to environmental cues.

Data availability

Data for this article will be available upon request. This manuscript will be available at **https://www.ekharlamgroup.com/**.

Conflicts of interest

There are no conflicts to declare.

Acknowledgements

This work is supported by NSF DMR Award #1904816. We acknowledge Dr Shahriar Habib and Dr Bing Xue for their technical assistance with sample preparation and microscopy measurements during their tenure at UAB. The UAB high-resolution imaging facility is acknowledged for the use of CLSM and SEM. This study is partly based on work supported under the IR/D Program by the National Science Foundation (E. K.). Any opinions, findings, conclusions, or recommendations expressed in this study are those of the author(s) and do not necessarily reflect the views of the National Science Foundation.

References

1 C. Kinnear, T. L. Moore, L. Rodriguez-Lorenzo, B. Rothen-Rutishauser and A. Petri-Fink, *Chem. Rev.*, 2017, **117**, 11476–11521.
2 D. B. Dusenbery, *J. Bacteriol.*, 1998, **180**, 5978.
3 K. D. Young, *Microbiol. Mol. Biol. Rev.*, 2006, **70**, 660–703.
4 S. S. Justice, D. A. Hunstad, L. Cegelski and S. J. Hultgren, *Nat. Rev. Microbiol.*, 2008, **6**, 162–168.
5 A. Brakhage, S. Bruns, A. Thywissen, P. Zipfel and J. Behnsen, *Curr. Opin. Microbiol.*, 2010, **13**, 409–415.
6 S. S. Justice, C. Hung, J. A. Theriot, D. A. Fletcher, G. G. Anderson, M. J. Footer and S. J. Hultgren, *Proc. Natl. Acad. Sci. U. S. A.*, 2004, **101**, 1333–1338.
7 B. Liu, M. Gulino, M. Morse, J. X. Tang, T. R. Powers and K. S. Breuer, *Proc. Natl. Acad. Sci. U. S. A.*, 2014, **111**, 11252–11256.
8 M. A. Constantino, M. Jabbarzadeh, H. C. Fu and R. Bansil, *Sci. Adv.*, 2016, **2**, e1601661.
9 Y. Shen, A. Siryaporn, S. Lecuyer, Z. Gitai and H. A. Stone, *Biophys. J.*, 2012, **103**, 146–151.
10 S. Cooper and M. W. Denny, *FEMS Microbiol. Lett.*, 1997, **148**, 227–231.
11 K. D. Young, *Curr. Opin. Microbiol.*, 2007, **10**, 596–600.
12 V. Kudryavtseva and G. B. Sukhorukov, *Adv. Mater.*, 2024, **36**, e2307675.
13 J. Yoo, D. Irvine, D. Discher and S. Mitragotri, *Nat. Rev. Drug Discovery*, 2011, **101**, 521–535.
14 J. A. Champion, Y. K. Katare and S. Mitragotri, *J. Controlled Release*, 2007, **121**, 3–9.
15 P. Decuzzi and M. Ferrari, *Biophys. J.*, 2008, **94**, 3790–3797.
16 J. Wang, J. D. Byrne, M. E. Napier and J. M. DeSimone, *Small*, 2011, **7**, 1919–1931.
17 J. Chen, V. Kozlovskaya, A. Goins, J. Campos-Gomez, M. Saeed and E. Kharlampieva, *Biomacromolecules*, 2013, **14**, 3830–3841.
18 L. Yang, Z. Zhou, J. Song and X. Chen, *Chem. Soc. Rev.*, 2019, **48**, 5140–5176.
19 I. Mirza and S. Saha, *ACS Appl. Bio Mater.*, 2020, **3**, 8241–8270.
20 P. E. Saw, X. Xu, M. Zhang, S. Cao, O. C. Farokhzad and J. Wu, *Angew. Chem., Int. Ed.*, 2020, **59**, 6249–6252.
21 I. A. B. Pijpers, L. K. E. A. Abdelmohsen, Y. Xia, S. Cao, D. S. Williams, F. Meng, J. C. M. van Hest and Z. Zhong, *Adv. Therap.*, 2018, **1**, 1800068.
22 C. K. Wong, A. F. Mason, M. H. Stenzel and P. Thordarson, *Nat. Commun.*, 2017, **8**, 1240.
23 Y. Xiao, A. Tan, A. W. Jackson and B. J. Boyd, *Chem. Mater.*, 2022, **34**, 2503–2530.
24 H. Safari, W. J. Kelley, E. Saito, N. Kaczorowski, L. Carethers, L. D. Shea, O. Eniola-Adefeso and O. Eniola-Adefeso, *Sci. Adv.*, 2020, **6**, eaba1474.
25 A. Arnida, M. M. Janát-Amsbury, A. Ray, C. M. Peterson and H. Ghandehari, *Eur. J. Pharm. Biopharm.*, 2011, **77**, 417–423.
26 P. Decuzzi, B. Godin, T. Tanaka, S. Y. Lee, C. Chiappini, X. Liu and M. Ferrari, *J. Controlled Release*, 2010, **141**, 320–327.
27 E. Ben-Akiva, R. A. Meyer, H. Yu, J. T. Smith, D. M. Pardoll and J. J. Green, *Sci. Adv.*, 2020, **6**, eaay9035.
28 D. M. Richards and R. G. Endres, *Proc. Natl. Acad. Sci. U. S. A.*, 2016, **113**, 6113–6118.
29 X. Hu, D. Zhang and S. S. Sheiko, *Adv. Mater.*, 2018, **30**, 1707461.
30 A. Brakhage, S. Bruns, A. Thywissen, P. Zipfel and J. Behnsen, *Curr. Opin. Microbiol.*, 2010, **13**, 409–415.
31 C. Matz, T. Bergfeld, S. A. Rice and S. Kjelleberg, *Environ. Microbiol.*, 2004, **6**, 218–226.
32 K. Jürgens, J. Pernthaler, S. Schalla and R. Amann, *Appl. Environ. Microbiol.*, 1999, **65**, 1241–1250.
33 T. Posch, J. Jezbera, J. Vrba, K. Simek, J. Pernthaler, S. Andreatta and B. Sonntag, *Microb. Ecol.*, 2001, **42**, 217–227.
34 M. Stasiuk, G. Kijanka and A. Kozubek, *Postepy Biochem.*, 2009, **55**, 425–433.
35 E. Sahai, *Nat. Rev. Cancer*, 2007, **7**, 737–749.
36 L. Mei, Y. Liu, H. J. Zhang, Z. Zhang, H. Gao and Q. He, *ACS Appl. Mater. Interfaces*, 2016, **8**, 9577–9589.
37 C. Anselmo, M. Zhang, S. Kumar, D. R. Vogus, S. Menegatti, M. E. Helgeson and S. Mitragotri, *ACS Nano*, 2015, **9**, 3169–3177.
38 H. Sun, E. H. Wong, Y. Yan, J. Cui, Q. Dai, J. Guo, G. G. Qiao and F. Caruso, *Chem. Sci.*, 2015, **6**, 3505–3514.
39 J. L. Perry, K. P. Herlihy, M. E. Napier and J. M. DeSimone, *Acc. Chem. Res.*, 2011, **44**, 990–998.
40 J. A. Champion, Y. K. Katare and S. Mitragotri, *Proc. Natl. Acad. Sci. U. S. A.*, 2007, **104**, 11901–11904.
41 L. Tao, X. M. Zhao, J. M. Gao and W. Hu, *Nanotechnology*, 2010, **21**, 095301.
42 P. Guo, D. Liu, K. Subramanyam, B. Wang, J. Yang, J. Huang, D. T. Auguste and M. A. Moses, *Nat. Commun.*, 2018, **9**, 130.

43 G. K. Such, A. P. R. Johnston and F. Caruso, *Chem. Soc. Rev.*, 2011, **40**, 19–29.
44 T. Mauser, C. Dejugnat and G. B. Sukhorukov, *J. Phys. Chem. B*, 2006, **110**, 20246–20253.
45 E. Kharlampieva, V. Kozlovskaya and S. A. Sukhishvili, *Adv. Mater.*, 2009, **21**, 3053–3065.
46 D. Gundogdu, C. Alemdar, C. Turan, H. Husnugil, S. Banerjee and I. Erel-Goktepe, *Colloids Surf., A*, 2023, **676**, 132213.
47 V. Kozlovskaya and E. Kharlampieva, *Macromol. Biosci.*, 2022, **22**(1), 2100328.
48 M. T. Cook, G. Tzortzis, V. V. Khutoryanskiy and D. Charalampopoulos, *J. Mater. Chem. B*, 2013, **1**, 52–60.
49 M. K. Blees, A. W. Barbard, P. A. Rose, S. P. Roberts, K. L. McGill, P. Y. Huang, A. R. Ruyack, J. W. Kevek, B. Kobrin, D. A. Muller and P. L. McEuen, *Nature*, 2015, **524**, 204–207.
50 S. P. Timoshenko and J. M. Gere, *Theory of elastic stability*, McGraw-Hill Book, New York, 1961.
51 W. Xu, K. S. Kwok and D. H. Gracias, *Acc. Chem. Res.*, 2018, **51**, 436–444.
52 J. F. Alexander, V. Kozlovskaya, J. Chen, T. Kuncewicz, E. Kharlampieva and B. Godin, *Adv. Healthcare Mater.*, 2015, **4**, 2657–2666.
53 V. Kozlovskaya, M. Dolmat and E. Kharlampieva, *Langmuir*, 2022, **38**, 7867–7888.
54 V. Kozlovskaya, B. Xue, M. Dolmat and E. Kharlampieva, *Macromolecules*, 2021, **54**, 9712–9723.
55 V. Kozlovskaya, J. Alexander, Y. Wang, T. Kuncewicz, X. Liu, B. Godin and E. Kharlampieva, *ACS Nano*, 2014, **8**, 5725–5737.
56 S. She, Q. Li, B. Shan, W. Tong and C. Gao, *Adv. Mater.*, 2013, **25**, 5814–5818.
57 S. Zhao, F. Caruso, L. Dähne, G. Decher, B. G. De Geest, J. Fan, N. Feliu, Y. Gogotsi, P. T. Hammond, M. C. Hersam, A. Khademhosseini, N. Kotov, S. Leporatti, Y. Li, F. Lisdat, L. M. Liz-Marzán, S. Moya, P. Mulvaney, A. L. Rogach, S. Roy, D. G. Shchukin, A. G. Skirtach, M. M. Stevens, G. B. Sukhorukov, P. S. Weiss, Z. Yue, D. Zhu and W. J. Parak, *ACS Nano*, 2019, **13**, 6151–6169.
58 B. V. Parakhonskiy, W. J. Parak, D. Volodkin and A. G. Skirtach, *Langmuir*, 2019, **35**, 8574–8583.
59 L. Van der Meeren, J. Li, B. V. Parakhonskiy, D. V. Krysko and A. G. Skirtach, *Anal. Bioanal. Chem.*, 2020, **412**, 5015–5029.
60 A. Sarode, A. Annapragada, J. Guo and S. Mitragotri, *Biomaterials*, 2020, **242**, 119929.
61 M. V. Zyuzin, A. S. Timin and G. B. Sukhorukov, *Langmuir*, 2019, **35**, 4747–4762.
62 M. T. Cabeen and C. Jacobs-Wagner, *Nat. Rev. Microbiol.*, 2005, **3**, 601–610.
63 T. Sugimoto, M. M. Khan and A. Muramatsu, *Colloids Surf., A*, 1993, **70**, 167–169.
64 T. Sugimoto, M. M. Khan, A. Muramatsu and H. Itoh, *Colloids Surf., A*, 1993, **79**, 233–247.
65 N. Gupta, V. Kozlovskaya, M. Dolmat and E. Kharlampieva, *Langmuir*, 2019, **35**, 10910–10919.
66 V. Kozlovskaya, S. Yakovlev, M. Libera and S. A. Sukhishvili, *Macromolecules*, 2005, **38**, 4828–4836.
67 V. Kozlovskaya, W. Higgins, J. Chen and E. Kharlampieva, *Chem. Commun.*, 2011, **47**, 8352–8354.
68 V. Kozlovskaya, Y. Wang, W. Higgins, J. Chen, Y. Chen and E. Kharlampieva, *Soft Matter*, 2012, **8**, 9828–9839.
69 S. A. Sukhishvili and S. Granick, *Macromolecules*, 2002, **35**, 301–310.
70 B. Xue, V. Kozlovskaya, F. Liu, J. Chen, J. Williams, J. Campos-Gomez, M. Saeed and E. Kharlampieva, *ACS Appl. Mater. Interfaces*, 2015, **7**, 13633–13644.
71 T. Bala, B. L. V. Prasad, M. Sastry, M. U. Kahaly and U. V. Waghmare, *J. Phys. Chem. A*, 2007, **111**, 6183–6190.
72 W. Wang, J. Zhu, Q. Huang, L. Zhu, D. Wang, W. Li and W. Yu, *Molecules*, 2024, **29**, 308.
73 O. Shchepelina, M. Lisunova, I. Drachuk and V. Tsukruk, *Chem. Mater.*, 2012, **24**, 1245–1254.